Polarized anionic phospholipids and exocytosis are implicated in the polarized recruitment of budding yeast AP180, an endocytic initiator

Paul Marchando, Gean Hu, Feng Yuan, Jordan M. Ngo, Yidi Sun, David G. Drubin*

16 Barker Hall, Dept. of Molecular and Cell Biology, University of California, Berkeley, CA 94720, USA.

* Corresponding author

phone: 510-642-3692, fax: 510-643-0062,
e-mail: drubin@berkeley.edu

Abstract

Understanding of the mechanisms that initiate clathrin-mediated endocytosis (CME) is incomplete. Recent studies in budding yeast identified the endocytic adaptor proteins Yap1801/Yap1802 (budding yeast AP180) as key CME factors that promote CME initiation in daughter cells during polarized growth, but how Yap1801/2 are recruited preferentially to the plasma membrane of daughter cells is not clear. The only known cargos for Yap1801/2 in yeast are the synaptobrevins Snc1 and Snc2, which serve as v-SNARES for exocytic vesicles reaching the plasma membrane and are crucial for polarized cell growth. In this study, we examine the spatiotemporal dynamics of functional, fluorescent protein-tagged Snc2 expressed from its endogenous locus and provide evidence that, along with anionic phospholipids, Snc2 specifically recruits Yap1802 to growing daughter cells. This protein-protein interaction creates a direct link between polarized secretion and CME and has further implications in CME initiation.

Introduction

While much research has focused on how clathrin-mediated endocytosis (CME) is initiated, consensus about the molecular mechanism has not been reached (Godlee and Kaksonen, 2013). Rab GTPases are known to initiate many trafficking processes, but no single trigger or pioneering factor for CME has been identified (Kreis *et al.*, 1995; Godlee and Kaksonen, 2013; Martin and Arkowitz, 2014), although membrane-bound cargo has been proposed to play a role (Taylor *et al.*, 2011; Goode *et al.*, 2015; Pedersen *et al.*, 2020).

In the budding yeast *Saccharomyces cerevisiae*, recent studies demonstrated that CME site initiation and maturation dynamics depend on position on the plasma membrane within a growing, polarized yeast cell (Layton *et al.*, 2011; Pedersen *et al.*, 2020; Sun *et al.*, 2024). Budding yeast proliferate by forming daughter cells, also referred to as “buds,” on the surface of a mother cell. Exocytosis is highly biased toward the daughter cell, so molecules delivered to the plasma membrane during exocytosis, such as SNARE proteins, are enriched near these exocytic sites (Field and Schekman, 1980). Since CME is the major pathway that retrieves material from the plasma membrane back into the cell interior, the presence of cargo concentrated in the bud

might affect CME site initiation or maturation (Carroll *et al.*, 2012; Cocucci *et al.*, 2012; Brach *et al.*, 2014). Indirect approaches have supported this possibility, but a direct link between polarized secretion and polarized CME (originally observed as polarized actin patches) has yet to be demonstrated (Adams and Pringle, 1984; Goode *et al.*, 2015; Pedersen *et al.*, 2020).

CME in budding yeast displays two temporal phases with distinct behaviors (Pedersen *et al.*, 2020). The transition between these phases coincides with differential Pan1 (budding yeast intersectin homolog) behavior in mother and daughter cells (Sun *et al.*, 2024). Pan1 undergoes a "low-abundance" phase followed by a "high-abundance" phase in mother cells, while only displaying the high-abundance phase in daughters (Sun *et al.*, 2024). We thus define early-arriving proteins as those that appear at CME sites before the high-abundance Pan1 phase, and late-arriving proteins as those that appear during or after the high-abundance Pan1 phase (Brach *et al.*, 2014; Bradford *et al.*, 2015; Sun *et al.*, 2015, 2017, 2024; Pedersen *et al.*, 2020). Early-arriving proteins show position-dependent differences in lifetimes (short and regular in daughters, longer and variable in mothers), while late-arriving proteins exhibit more regular lifetimes regardless of cell growth stage or position within the cell (Pedersen *et al.*, 2020; Sun *et al.*, 2024).

This heterogeneity in CME site behavior is partly driven by the endocytic adaptor complex AP180 (Yap1801 and Yap1802 in yeast, abbreviated as Yap1801/2) (Sun *et al.*, 2024). Yap1801/2 interact cooperatively with the FCHo1/2 homolog Syp1 to recruit the EPS15 homolog Ede1 to the bud cortex, initiating the early stages of CME (Lu and Drubin, 2017; Sun *et al.*, 2024). Yap1801/2 are polarized strongly to the bud during yeast cell growth while mother cells have nearly undetectable Yap1801/2, explaining the observed position-dependent differences in CME initiation rates and lifetimes (Sun *et al.*, 2024). While Yap1801/2's role in CME initiation as perhaps the earliest acting factor is more clear, the factors upstream of Yap1801/2 recruitment remain speculative (Sun *et al.*, 2024).

Yap1801/2 have one known cargo, the v-SNAREs Snc1 and Snc2 (abbreviated as Snc1/2), homologs of the mammalian synaptobrevins, which depend of CME for their retrieval from the plasma membrane (Burston *et al.*, 2009; Miller *et al.*, 2011). Snc1/2 are the only known v-SNAREs in budding yeast that facilitate the fusion of secretory vesicles with the plasma membrane (Burri and Lithgow, 2004). In addition to binding Snc1/2, Yap1801/2 can directly bind anionic lipid species (Ford *et al.*, 2001). Since both Snc1/2 and anionic lipid species, particularly phosphatidylserine, are enriched in daughter cells, Snc1/2 and anionic lipids are poised to play a role in the asymmetrical behavior of Yap1801/2 in yeast undergoing bud growth (Burston *et al.*, 2009; Sun and Drubin, 2012; Meca *et al.*, 2019). The residues in Yap1801/2 mediating both binding activities are well characterized, and precise perturbation of both Snc1/2 and lipid binding could reveal if both are equally important for Yap1802 recruitment or if one overshadows the other.

The yeast synaptobrevins Snc1/2 thus provide a unique opportunity to study the earliest stages of CME and better characterize a yeast CME cargo, a task that has remained difficult and yielded mixed results in past studies (Toshima *et al.*, 2006; Carroll *et al.*, 2009). Using live-cell

89 microscopy, we compare the behaviors of fluorescent Snc1 and Snc2 expressed from their
90 natural chromosomal loci and provide the first spatiotemporal analysis of Snc2 expressed at
91 endogenous levels. This analysis highlights a complex relationship between Snc2 and CME,
92 which varies depending on the cell growth stage. Additional experiments show that Snc2 and
93 anionic phospholipids collaborate to recruit the endocytic adaptor Yap1802 to daughter cells
94 during growth, linking polarized secretion to CME initiation.

Results and Discussion

Functional GFP-tagged Snc2 fusion protein expressed from its endogenous genomic locus displays complex spatiotemporal behaviors relative to the CME machinery

To analyze the spatial distribution of Snc1 and Snc2 in yeast cells, we created in-frame fusions of the corresponding genes at their endogenous genomic loci with sequences encoding GFP and visualized the N-terminally-tagged fluorescent fusion proteins in cells by Airyscan (Zeiss) confocal microscopy (Figure 1A, Figure S1A, arrows). The two proteins displayed similar subcellular localization, appearing preferentially in growing daughter cells, in agreement with previous studies of overexpressed Snc1, and they both decorated internal structures that are presumably membrane-bound organelles (Gurunathan *et al.*, 2000, 2002; Lewis *et al.*, 2000; Valdez-Taubas and Pelham, 2003; Burston *et al.*, 2009). The GFP-Snc1 fusions displayed weak signals, consistent with the low signal observed on immunoblots, suggesting a greater abundance of Snc2 (Figure S2A). In addition, *snc2Δ* strains were more severely impaired in growth than *snc1Δ* strains (Figure S2B). *SNC2* transcripts outnumber *SNC1* transcripts by nearly threefold, perhaps explaining the differential behaviors even though the paralogs display 76% sequence identity (Katz *et al.*, 1998; Grote *et al.*, 2000; Gurunathan *et al.*, 2000; Lipson *et al.*, 2009). Due to the greater abundance and importance of Snc2 for cell growth, we focus on GFP-Snc2 henceforth. Since GFP-Snc2 expressed from the endogenous promoter was able to rescue the growth defects of *snc2*Δ cells, we conclude that this fusion protein is functional and likely to serve as a faithful reporter of the spatiotemporal dynamics of these v-SNARES (Figure S2B).

We next studied the complex behaviors and interactions of Snc2 with the CME machinery (reported by Sla1-mScarlet) in live cells using Nikon Spatial Array Confocal (NSPARC) microscopy at sub-second temporal resolution (Supplemental Videos 1 and 2) (Delattre, 2023). Snc2 and Sla1 both showed preferential enrichment at the plasma membrane in daughter cells (Figure 1B, Figure S1B, arrows). Snc2 displayed a mixture of diffuse and punctate signals while Sla1 appeared solely in puncta (Figure 1A, B, Figure S1A, B). Bright Snc2-positive compartments, possibly early endosomes, translated across large lengths of budded daughter cells in several seconds, moving from the plasma membrane through the cell interior and returning to the plasma membrane surface (the same cell and event is depicted in Figure 1C, white arrows, and Supplemental Video 1, arrows). This type of motion is consistent with the known Snc2 retrograde transport to the trans-Golgi network (TGN), fusion with endosomes, and delivery back to the plasma membrane (Gurunathan *et al.*, 2000; Lewis *et al.*, 2000; Burri and Lithgow, 2004; Best *et al.*, 2020). Additionally, punctate cytoplasmic structures moved directionally from mother cells toward daughter cells, consistent with their participation in polarized secretion (Figure 1C, yellow arrows, Supplemental Video 1, arrows).

Using circumferential kymographs created by tracing the outline of the plasma membrane on the vertical axis and projecting the outline through time on the horizontal axis, we better observed how Snc2-positive compartments interact with the plasma membrane and the CME machinery in mother vs. daughter cells (Figure 1D, Figure S1C-E) (Lu and Drubin, 2017; Sun *et al.*, 2017). In daughter cells, GFP-Snc2 appeared on the plasma membrane diffusely, highlighted

139 by the background haziness observed throughout kymographs in Figure 1D (top row) and Figure
140 S1C when compared to other growth stages. Within these kymographs, bright traces of Snc2-
141 positive compartments appeared and disappeared (Figure 1D, white arrows, Figure S1C),
142 coinciding with the Snc2-positive compartments observed in Figure 1C and Supplemental Video
143 1 that transiently interacted with the plasma membrane. While these bright Snc2-positive
144 traces did generally overlap with Sla1 traces (Figure 1D, white arrows, Figure S1C), the high Snc2
145 background precludes any direct functional interpretations. In kymographs of mother cells, Snc2
146 puncta translated laterally across the plasma membrane, occasionally coinciding with the
147 internalization of endocytic vesicles (Figure 1D, yellow arrows, Figure S1D). Unbudded cells
148 displayed a mixture of these behaviors, with brighter traces that fluctuate less in intensity and
149 show longer lifetimes (Figure 1D, third row, Figure S1E). On rare occasions, Snc2-positive
150 punctate traces were observed to track and disappear with Sla1 in a manner consistent with
151 CME cargo behavior (Figure 1D, cyan arrows).
152
153 CME perturbation highlights a clear dependency of Snc2 on CME for internalization. Treatment
154 of yeast cells with the Arp2/3 complex inhibitor CK-666 halted endocytic internalization (Hetrick
155 *et al.*, 2013) and trapped Snc2 preferentially on the plasma membrane in daughter cells while
156 Snc2 cytoplasmic puncta disappeared (Figure 1E). In these cells, stalled endocytic sites, marked
157 by Sla1-mScarlet, appeared as stationary puncta on the plasma membrane, although Snc2 signal
158 was not noticeably enriched at these puncta. Upon CK-666 washout, Snc2 could again be seen
159 on cytoplasmic puncta and appeared brighter, perhaps due to the drug-induced local Snc2
160 enrichment in daughter cells (Figure 1E). Using NSPARC microscopy to observe the restart of
161 CME following CK-666 washout with greater spatial and temporal resolution, we more clearly
162 visualized the direct interaction of Snc2 and Sla1-positive traces (Figure S1F). Kymographs of
163 videos acquired directly following CK-666 washout showed increased Snc2/Sla1 colocalization
164 and coincident internalization when compared to unperturbed cells (Figure S1F, white arrows).
165 These kymographs additionally suggested a slight enrichment of Snc2 at stalled Sla1 puncta,
166 demonstrated by the colocalizing parallel traces observed before CME resumes (Figure S1F,
167 yellow arrows). These observations suggest that, in daughter cells, Snc2 tracks and internalizes
168 with the CME machinery like the other canonical CME components, but the superimposed
169 background signal from other stages of Snc2's complex recycling cycle obscures this behavior at
170 steady state. Observing cargo associated with CME sites is notoriously difficult due to signal-to-
171 noise challenges as cargo saturate CME sites and accumulate on the plasma membrane.
172
173 These combined results suggest a complex interplay between the dynamic Snc2 life cycle and
174 CME. Our time-lapse data are consistent with the known functions of Snc2 in polarized
175 secretion and in retrograde transport of endosomes back to the TGN, but the high-speed
176 dynamics of these behaviors and the coincident endocytic internalization of Snc2 with Sla1 are
177 newly reported here. Of particular interest is the observed interaction of cytosolic Snc2-positive
178 compartments with plasma membrane-bound Sla1 traces. These Snc2-positive puncta appear
179 to move to and from the plasma membrane in a coordinated manner, as if collecting newly
180 budded endosomes from CME sites (Figure 1D, yellow arrows, Supplemental Video 2, arrows).
181 This "vacuum cleaner" behavior has also been observed between labeled endosomes and
182 endocytic sites in our previous studies using both fluorescent alpha factor endocytic cargo

183 (Toshima *et al.*, 2006) and the lipophilic dye FM 4-64 (Cortesio *et al.*, 2015). These events could
184 represent endosomes that fuse with nascent endocytic vesicles via Snc2's SNARE activity, but
185 whether SNARE function plays an active role in this behavior remains to be investigated.
186 Nonetheless, this behavior suggests a high level of spatial and temporal coordination between
187 CME vesicle internalization and subsequent fusion with early endosomes, and we believe the
188 strains created here can aid further investigation of this mechanism.
189
190 *Snc2 internalization from the cell surface via CME is important for cell viability*
191
192 Previous work on the mammalian synaptobrevins identified residues that mediate their
193 interaction with the endocytic adapter CALM, a mammalian homolog of Yap1801/2 (Grote *et*
194 *al.*, 2000; Gurunathan *et al.*, 2000; Miller *et al.*, 2011). The residues important for this
195 interaction correspond to V39 and M42 on Snc2. Alanine substitutions at these residues did not
196 affect Snc2 expression in both *SNC1* and *snc1Δ* backgrounds (Figure S2C) but resulted in diffuse
197 Snc2 signal on the plasma membrane in both daughter and mother cells, consistent with an
198 internalization defect and similar to the phenotype observed when endocytosis is stalled with
199 CK-666 (Figure 1F) (Grote *et al.*, 2000; Shen *et al.*, 2013). This result suggests that the V39A
200 M42A Snc2 mutant is still competent to mediate exocytosis, Snc1/2's essential function, and
201 that CME of more lowly-expressed Snc1 alone is sufficient for yeast to remain healthy in
202 standard conditions. We tested the latter conclusion in an *snc1Δ* background, wherein the Snc2
203 mutant again showed diffuse plasma membrane staining in mother and daughter cells, but
204 these cells displayed a severe growth defect, irregular morphologies, and diffuse Snc2
205 cytoplasmic signal consistent with vacuolar fragmenting or sorting defects observed in
206 unhealthy cells (Figure 1F, S2B) (Grote *et al.*, 2000; Stauffer and Powers, 2015). These
207 observations differ from previous findings, which show reduced Snc2 M42A protein levels by
208 immunoblot compared to wild-type Snc2, and no growth defect in snc1Δ snc2 M42A cells. This
209 result suggests that the V39A M42A Snc2 mutant expressed natively shows decreased Snc2
210 protein levels but is not harmful in an snc1Δ background (Grote *et al.*, 2000). This discrepancy
211 could be explained by the prior introduction of the *SNC2* coding sequence, with 500 flanking
212 base pairs on either side of the open reading frame, at the *LEU2* locus, rather than at the native
213 chromosomal locus (Grote *et al.*, 2000). Perhaps there are regulatory sequences beyond these
214 500 base pairs at the native locus that impact *SNC2* expression. Given our observed roughly 7-
215 fold difference in Snc1 and Snc2 protein abundance but only 3-fold difference in RNA
216 expression, there may be differences in the expression and translation of these native loci and
217 transcripts that have yet to be uncovered (Figure S2A) (Lipson *et al.*, 2009).
218
219 These observations indicate that CME of some Snc1/2 molecules is essential for normal cell
220 physiology. While it is possible that the V39A M42A mutation impacts other cellular processes
221 in which Snc2 is involved, the conserved methionine residue has been shown to specifically
222 mediate the interaction of synaptobrevins with CALM/AP180, and previous studies
223 demonstrated that CME of SNAREs and their ability to mediate exocytosis are separable
224 activities (Miller *et al.*, 2011; Ma and Burd, 2019).
225
226 *Roles for polarized anionic phospholipid and Snc2 localization in polarized Yap1802 recruitment*

227
228 We next created specific point mutations in Yap1802 to investigate the relationship between
229 Yap1802, Snc2, and negatively charged lipid species during polarized growth. Residues of the
230 mammalian Yap1802 homolog CALM that mediate its interaction with anionic phospholipids
231 and synaptobrevins have been characterized and fall within its ANTH (AP180 N-terminal
232 homology) domain (Ford *et al.*, 2001; Miller *et al.*, 2011; Pashkova *et al.*, 2021). The analogous
233 residues in *S. cerevisiae* Yap1802 correspond to lysines 21 and 23 for lipid interaction and
234 leucine 203 for Snc2 interaction (Figure 2A, B) (Ford *et al.*, 2001; Sun *et al.*, 2005; Miller *et al.*,
235 2011; Pashkova *et al.*, 2021). Alphafold2 multimer analysis strengthened confidence that L203
236 in Yap1802 interacts with M42 in Snc2 (Figure 2B) (Mirdita *et al.*, 2022). Using a CRISPR/Cas9-
237 based approach to generate yap1802 K21E K23E and L203S mutants, we tested whether
238 interactions of Yap1802 with anionic phospholipids and plasma membrane-bound Snc2 might
239 facilitate Yap1802 recruitment to growing daughter cells (Anand *et al.*, 2017). Given the high
240 degree of homology between Yap1801 and Yap1802, the observation that Yap1802 is
241 functionally sufficient in *yap1801Δ* cells, and the strong polarization of Yap1802 to small- and
242 medium-sized daughter cells, we decided to conduct experiments on point-mutated Yap1802
243 mutants in a *yap1801Δ* background (Sun *et al.*, 2024). The mutated strains showed no
244 detectable difference in Yap1802 expression levels and did not cause an observable
245 temperature-sensitive cell viability defect (Figure S2D, E). Liposome flotation assays confirmed a
246 lipid binding defect for the yap1802 K21E K23E ANTH domain, which is evident at various
247 concentrations of the mutant YAP1802 ANTH domain compared to the wild-type YAP1802 ANTH
248 domain (Figure S2F).
249
250 Yeast strains individually expressing the yap1802 K21E K23E mutant (predicted to be defective
251 in lipid binding), the yap1802 L203S mutant (predicted to be defective in Snc2 binding), or the
252 yap1802 3x PM (K21E K23E L203S, predicted to be defective in both lipid and Snc2 binding) each
253 displayed a Yap1802 recruitment defect, which can be best visualized using maximum intensity
254 projections of time-lapse movies (Figure 2C). In these projections, quantification of the mean
255 cortex fluorescence intensity in daughter cells showed a decrease in plasma membrane Yap1802
256 signal among all point mutants tested (Figure 2E). Additionally, looking closer at these cortex
257 intensity traces in daughter cells revealed a unimodal curve with a maximum near the middle of
258 the trace, coinciding with the very tip of the growing bud (Figure S3A). Each individual mutant
259 lost this curved Yap1802 trace and showed reduced intensity along the length of each trace.
260 Individual Yap1802 endocytic events in budded cells were still observed in each mutant, with
261 the lipid and Snc2 mutants maintaining normal lifetimes compared to cells expressing wild-type
262 Yap1802 (Figure 2D, 2F). However, the lifetimes of yap1802 3x PM-GFP events were significantly
263 shorter than those for the wild-type cells and individual mutants (Figure 2F). These 3x PM
264 lifetimes are consistent with those observed in strains that lack the ability to localize Ede1
265 properly, such as *yap1801Δ/yap1802Δ* double null mutants and *ede1Δ* cells (Brach *et al.*, 2014;
266 Sun *et al.*, 2024). Since Yap1802 is required for proper Ede1 localization, this observation
267 suggests that a major part of Yap1802's membrane-binding ability is contained within these
268 three residues in its ANTH domain. We note that in Figure 2C yap1802 3x PM-GFP shows an
269 elevated signal at the bud neck, which is representative of the localization for this mutant. We
270 speculate that since yap1802 3x PM-GFP is defective in both lipid and Snc2 binding, it is

271 recruited to the bud neck by Ede1 through Yap1802's NPF motifs because Ede1 is concentrated
272 at the bud neck (Stimpson *et al.*, 2009). Two-color imaging of the 3x PM and Ede1 confirmed
273 strong colocalization between the two proteins at the bud neck (Figure S3C).
274
275 Since perturbing Yap1802's interaction with lipids and cargo (Snc2) led to abnormal Yap1802
276 behavior, we investigated whether these endocytic perturbations also led to abnormal Snc2
277 behavior. Using confocal microscopy to visualize endogenously expressed mScarlet-Snc2 in yeast
278 strains expressing point-mutated Yap1802-GFP fusion proteins, we observed differential
279 distributions of Snc2 on the plasma membrane (Figure 2G). *yap1801Δ YAP1802* cells displayed
280 normal Snc2 localization when compared to wild-type cells (compare Figure 2G with 1B), but
281 each point mutant led to defects in Snc2 internalization, with an increase in Snc2 cortex signal in
282 mother cells across all conditions (Figure 2H, Figure S3B). The Yap1802 K21E K23E mutant still
283 shows a polarized distribution of Snc2 compared to other point mutants, but it also exhibits
284 more plasma membrane signal in mothers compared to cells expressing wild-type Yap1802
285 (Figure 2G, H). This indicates that the Yap1802 K21E K23E mutant can still bind and internalize
286 with Snc2 via CME, but the overall efficiency of this process is reduced, likely due to decreased
287 lipid binding. This aligns with the reduced plasma membrane recruitment observed in the
288 Yap1802 K21E K23E mutant (Figure 2C) and may lead to less Snc2 uptake via CME. Additionally,
289 the largely plasma membrane-bound localization of Snc2 in the yap1802 L203S mutant further
290 confirmed that the L203 residue of Yap1802 plays a key role in internalizing Snc2 through
291 specific interactions (Figure 2G).
292
293 Taken together, these findings identify anionic phospholipids and Snc2 as important factors
294 facilitating the recruitment of Yap1802 to the daughter plasma membrane. Since wild-type
295 Yap1802 interacts with Snc2 directly and is most concentrated at the daughter cell tip where
296 exocytosis is most active, Yap1802 localization is directly linked to polarized cell growth and
297 secretion (Figure 3A). Signaling initiated by Cdc42 causes actin cable assembly from the
298 daughter cell tip, enabling a type V myosin to recruit many cellular components, including
299 secretory vesicles and the exocyst vesicle tethering complex to the bud tip (Figure 3A) (Pruyne
300 and Bretscher, 2000a, 2000b; Mei and Guo, 2018; Mei *et al.*, 2018). Once vesicles reach the
301 plasma membrane, we suggest that Snc2 and anionic phospholipids act together as a "landing
302 pad" for Yap1802, creating favorable conditions for its recruitment to the plasma membrane.
303 Since Yap1802's lipid binding and Snc2 binding display roughly equal importance for Yap1802
304 recruitment, we suggest that robust Yap1802 localization relies on its coincidence detection of
305 these two factors (Figure 3B). Recent work has suggested that Yap1801/2 may be among the
306 earliest-acting factors in polarized endocytosis, implicating this Yap1802/Snc2 interaction in the
307 initiation of CME in daughter cells during cell growth (Sun *et al.*, 2024). It seems likely that these
308 properties would also be conserved for the highly homologous paralogs Yap1801 and Snc1, but
309 this possibility remains to be tested.
310
311 Interestingly, we could not precisely perturb the endocytic machinery in a way that led to cell
312 growth defects like those observed in *snc2 V39A M42A/snc1Δ* cells. Since *yap1801Δ/yap1802Δ*
313 double null cells also display essentially normal growth and viability, this result suggests the
314 existence of adaptor proteins in addition to Yap1801/2 that can mediate Snc1/2 internalization,

315 perhaps AP2 or Syp1 (Figure S2D) (Sun *et al.*, 2024). In addition, the Hip1/R homolog Sla2, which
316 also contains an ANTH domain, and the epsins Ent1/2, could be candidates for this role.
317 However, since *sla2Δ* and *ent1Δ/ent2Δ* cells are completely defective in CME, and since our
318 efforts to identify Sla2 or Ent1/2 residues that might mediate interactions between these
319 proteins and Snc1/2 using Alphafold2 multimer analysis were not successful, studying the effect
320 these proteins have on Snc1/2 internalization must await future studies and new approaches
321 (Sun *et al.*, 2005; Maldonado-Báez *et al.*, 2008; Mirdita *et al.*, 2022).
322
323 *Conclusions*
324
325 Here, we provide evidence that the previously identified interactions between the endocytic
326 adaptor Yap1802, the CME cargo Snc2, and anionic phospholipids provide a direct link between
327 polarized cell growth driven by localized exocytosis and CME. The polarized delivery of Snc2 to
328 the plasma membrane by exocytosis and the subsequent endocytosis of these proteins appear
329 to be highly coordinated, as CME sites are concentrated near sites of localized exocytosis.
330 Additionally, given the recent identification of Yap1801/2 as among the earliest-acting factors in
331 CME, the Yap1802/Snc2 interaction could be involved in CME initiation. As the proteins
332 investigated here are highly conserved in all eukaryotes, we expect that our observations and
333 conclusions will prove relevant to other settings involving polarized secretion and efficient
334 compensatory cargo retrieval via CME, such as at presynaptic nerve termini (Saheki and Camilli,
335 2012).
336

337 **Materials/Methods**
338
339 *Strains, yeast husbandry, cloning, and plasmids*: All yeast strains produced and analyzed in this
340 study can be found in Table S1. All strains were derived from the wild-type diploid DDY1102 and
341 were propagated using standard yeast husbandry techniques (Amberg *et al.*, 2005). Genes
342 encoding C-terminally-tagged fusion proteins were engineered as previously described
343 (Longtine *et al.*, 1998). Genes encoding N-terminally tagged Snc2 fusion proteins were
344 engineered by cloning the genomic *SNC2* open reading frame (ORF) into a pFA6a-XFP backbone
345 to create an in-frame fusion protein. PCR products with homology to the *SNC2* locus were
346 generated from these plasmids, and then transformed into an *snc2Δ* background using
347 previously described techniques (Longtine *et al.*, 1998). The snc2 V39A M42A double mutant
348 was made at the endogenous *SNC2* locus by introducing the appropriate mutations into the
349 above plasmids using quick-change mutagenesis (Kunkel, 1985). Similarly, the yap1802 L203S
350 mutant was made by introducing the appropriate mutation into the wild-type gene carried on a
351 pFA6a-GFP backbone, then transforming the resulting PCR product into a *yap1802Δ* strain using
352 previously described techniques (Longtine *et al.*, 1998). All other point mutations were
353 introduced using CRISPR-Cas9 (Anand *et al.*, 2017). All plasmids can be found in Table S2.
354
355 *Yeast chemical fixation*: Yeast strains were grown overnight to mid-log phase (roughly OD 0.2-
356 0.4) in synthetic minimal media and fixed according to previous protocols in 4%
357 paraformaldehyde solution in cytoskeleton buffer (Kaplan and Ewers, 2015).
358
359 *Live-cell imaging*: Yeast strains were grown overnight to mid-log phase (roughly OD 0.2-0.4) in
360 synthetic minimal media lacking tryptophan (imaging media, containing L-histidine, L-leucine,
361 uracil, L-lysine, adenine, L-methionine, and 2% glucose), then adhered to 8-well imaging
362 chambers (Cellvis C8-1.5H-N) or glass coverslips using 0.2 mg/ml Concanavalin A. *GFP-snc2*
363 *V39A M42A/snc1Δ* strains were grown overnight to mid-log phase in casamino acid media
364 lacking tryptophan (0.17% yeast nitrogen base, 0.5% casamino acid, 0.5% ammonium sulfate,
365 uracil, adenine, and 2% glucose) (Kurokawa *et al.*, 2013). For CK-666 experiments, adhered cells
366 were treated for 30 min. with 50 µM CK-666 in imaging media. Media was aspirated and
367 washed once with imaging media before immediately commencing imaging. All imaging
368 experiments were repeated a minimum of two times with biological replicates (one mat a and
369 one mat alpha strain) with datapoints consisting either of individual cell intensity traces or
370 individual endocytic events, as per figure legends.
371
372 Widefield microscopy was performed using a Nikon Eclipse Ti microscope equipped with a
373 Nikon 100× 1.4 NA Plan Apo VC oil objective and a Neo 5.5 sCMOS camera from Andor
374 Technology. GFP/mScarlet two-color imaging was performed using a Lumencore Spectra X LED
375 light source with a Semrock FF-493/574-Di01 dual-pass dichroic and an FF01-524/628-25 dual-
376 pass excitation filter. Nikon Elements software was used to control the system, and all imaging
377 was done at room temperature (23°C).
378
379 Confocal imaging was performed using a Zeiss LSM 900 with Airyscan 2.0 detection equipped
380 with a 60x 1.4 NA oil objective. 1x averaging was used for all acquisitions. Excitation laser

381 wavelengths of 488 nm for GFP and 561 nm for mScarlet were used. Zeiss Zen Blue software
382 was used to control the system, and imaging was performed at 25°C using a temperature-
383 controlled chamber.
384
385 NSPARC confocal imaging was performed using a Nikon Eclipse Ti2 microscope equipped with a
386 60x 1.4 NA Plan Apo λD oil objective and an NSPARC (Nikon Spatial Array Confocal) detector. For
387 the 488 nm laser, an emission range of 503-545 nm was used, and for the 561 nm laser, an
388 emission range of 582-618 nm was used. All data were acquired in Galvo mode with a pinhole
389 size of 18 µM.
390
391 *Immunoblotting*: All protein samples were prepared from cells grown to mid-log phase using
392 trichloroacetic acid (TCA) precipitation (Pedersen and Drubin, 2019). 10% SDS-polyacrylamide
393 gels were run at 100 V and transferred to nitrocellulose membranes at 35 V for 12 hrs. Cells
394 were blocked in 5% milk in PBS, primary antibodies were prepared in PBS with 0.05% milk and
395 0.1% Tween-20, and secondary antibodies were prepared in PBS with 0.005% milk and 0.1%
396 Tween-20. All incubations occurred at RT for 1 hr with 3 x 5 min PBS washes in between. The
397 following primary antibodies were used in this study: mouse anti-GFP 1:500 (RRID:AB_390913,
398 11814460001, Roche), mouse anti-V5 1:2,000 (RRID:AB_2792973, R960CUS, Thermo Fisher
399 Scientific), rabbit anti-hexokinase 1:10,000 (RRID:AB_219918, 100-4159, Rockland), and mouse
400 anti-PGK1 1:10,000 (RRID:AB_2532235, 459250, Thermo Fisher Scientific). Immune blots were
401 probed with LICOR fluorophore-conjugated secondary antibodies and imaged on a LICOR
402 Odyssey CLx.
403
404 *Purification of Yap1802 ANTH truncations*: Expression and purification of wild-type ANTH (ANTH
405 WT) and its K21E K23E mutant were carried out as follows. Plasmids encoding either ANTH WT
406 or ANTH K21E K23E were transformed into *E. coli* BL21(DE3) competent cells. Following
407 transformation, cells were cultured in 1 L of 2×YT medium at 37°C with shaking at 220 rpm until
408 the optical density at 600 nm (OD_{600}) reached ~0.8. Protein expression was induced by adding 1
409 mM IPTG, and the cultures were incubated overnight at 18°C with shaking at 220 rpm. Cells
410 were harvested by centrifugation at 4°C and resuspended in 40 mL of lysis buffer containing 25
411 mM HEPES (pH 7.4), 150 mM NaCl, 20 mM imidazole, 10 mM β-mercaptoethanol (β-ME), 1%
412 Triton X-100, and one EDTA-free protease inhibitor tablet (Sigma-Aldrich). Cells were lysed by
413 sonication on ice, and the lysates were clarified by centrifugation at 40,000 rpm for 40 minutes
414 at 4°C. ANTH WT and K21E K23E proteins were found in the insoluble fraction. The pellets were
415 resuspended in denaturing buffer (8 M urea, 25 mM HEPES pH 7.4, 150 mM NaCl, 20 mM
416 imidazole) and centrifuged again under the same conditions. The denatured proteins, now in
417 the supernatant, were incubated with Ni-NTA resin (G Biosciences, USA) for 1 hour at 4°C with
418 gentle mixing. The resin was transferred to a gravity flow column and washed with the same
419 urea-containing buffer. Bound proteins were eluted using elution buffer consisting of 25 mM
420 HEPES, 150 mM NaCl, 250 mM imidazole, and 8 M urea (pH 7.4). Eluted proteins were gradually
421 refolded by stepwise dialysis into buffers containing decreasing concentrations of urea (6 M, 4
422 M, 2 M, and finally 0 M) in 25 mM HEPES, 150 mM NaCl (pH 7.4) at 4°C overnight. The final
423 protein products were aliquoted, flash-frozen in liquid nitrogen, and stored at -80°C.
424

425 *Purification of recombinant His$_6$-HaloTag*: His$_6$-HaloTag was purified using the protocol in Ngo et
426 al. 2025, with the following modifications. His$_6$-HaloTag was cloned into a pET28a vector and
427 expressed in *E. coli* Rosetta2(DE3)pLysS cells. A pre-culture (2.5 ml) was grown overnight at 37°C
428 and diluted to a 250 ml culture. The culture was incubated at 37°C until the OD_{600} reached 0.6,
429 and protein expression was induced upon addition of 50 µM IPTG for 4 hr at 37°C. The cells
430 were harvested by centrifugation at 5,000xg for 10 min at 4°C, and the cell pellet was stored at -
431 80°C until use. All subsequent manipulations were performed at 4°C. The cell pellet was thawed
432 on ice, resuspended in 7.5 ml of cold Ni-NTA lysis buffer (20 mM Tris-HCl pH 8.0, 300 mM NaCl,
433 10 mM imidazole, 2 mM $MgCl_2$, and a protease inhibitor cocktail) and sonicated 5 times (5 sec
434 on, 15 sec off, 20% power) using a Branson Sonifier 450. The lysate was clarified by
435 centrifugation at 20,000xg for 20 min in a fixed angle FIBERlite F21-8x50y rotor, and the
436 supernatant fraction was applied to a gravity flow column containing 0.5 ml of pre-equilibrated
437 HisPur^{TM} Ni-NTA Resin (Thermo Fisher Scientific). The column was washed with three column
438 volumes of cold Ni-NTA wash buffer (similar recipe as Ni-NTA lysis buffer but with 25 mM
439 imidazole) and eluted with 1.5 ml of cold Ni-NTA elution buffer (similar recipe as Ni-NTA lysis
440 buffer but with 300 mM imidazole). The imidazole eluate was buffer exchanged into tris-
441 buffered saline (TBS) using a HiTrap desalting column (Cytiva). The purified His$_6$-HaloTag was
442 distributed into aliquots, snap-frozen in liquid nitrogen, and stored at -80°C until use.
443
444 *Liposome preparation and sucrose density gradient flotation assays*: Liposomes were prepared
445 essentially as described in Williams et al., 2025, with the following modifications. Lipids (Avanti
446 Polar Lipids) were mixed in a glass vial at the following ratios: 38% DOPC, 20% POPE, 20% DOPS,
447 3% PI(4,5)P_2, 0.5% TexasRed-PE, and 18.5% cholesterol in 500 µl of 95% chloroform and 5%
448 methanol. The lipid mixture was briefly placed in an incubator preheated to 60°C before being
449 transferred to a vacuum chamber to evaporate the organic solvent. The dried lipids were
450 hydrated in 500 µl of TBS via incubation at 60°C for 30 min with intermittent vortexing. The
451 liposome suspension was then extruded through a polycarbonate filter of 200-nm pore size
452 (Whatman). For sucrose density gradient flotation assays, binding reactions (60 µl) consisted of
453 liposomes (20 µl), purified HaloTag (15-100 nM) or ANTH protein (see Table S3 for all Halo-Tag
454 concentrations used and for computed concentrations of each ANTH mutant using
455 densitometry), and TBS. The reactions were incubated at room temperature for 15 min, mixed
456 with 60 µl of 60% sucrose in TBS (for a final concentration of 30% sucrose), and sequentially
457 overlaid with 100 µl of 25% sucrose in TBS and 20 µl of TBS. The resulting sucrose step gradients
458 were centrifuged in a TLA100 rotor (Beckman) at 100,000 rpm (436,000xg) for 10 min at 4°C.
459 The floated liposomes were collected, and the amount of fluorescent lipid recovered was
460 quantified using a Tecan Infinite M Plex plate reader (Tecan). The bound proteins were
461 analyzed by SDS-PAGE and immunoblotting after adjusting the sample volume to normalize for
462 lipid recovery. Antibodies used for immunoblotting were mouse anti-6*His (RRID:AB_2923721,
463 66005-1-Ig, Proteintech) with sheep anti-mouse secondary (RRID:AB_772209, NXA931, Cytiva)
464 and mouse anti-His-Tag HRP conjugate (RRID:AB_2797714, 9991, Cell Signaling Technology).
465 Blots were developed with chemiluminescence and imaged on a BioRad ChemiDoc. Replicates
466 from both primary antibodies were combined for relative protein binding measurements, and
467 replicates using only the Proteintech antibody were used for concentration calibration and
468 binding fraction measurements.

469
470 *Image and data analysis (code availability)*: Montages and kymographs were generated using
471 custom scripts in Fiji (NIH) as well as the open-source cell segmentation package CellPose
472 (Stringer *et al.*, 2021; Sun *et al.*, 2024, 2017; Lu and Drubin, 2017). Line trace intensity data for
473 Yap1802 point mutants was analyzed using custom MATLAB scripts. Line traces of medium-
474 budded cells were generated using CellPose, then each intensity profile was interpolated to
475 match the length of the mean trace length. Intensity profiles were averaged at each length and
476 plotted using the MATLAB package plot_areaerrorbar (Martínez-Cagigal, 2024). Moving
477 arrowheads in supplemental movies were added using the Draw_Arrows plugin (Daetwyler *et*
478 *al.*, 2020). Plots were generated with MATLAB and GraphPad Prism 10. All code is available at
479 https://github.com/DrubinBarnes/Marchando_2024_Snc and https://github.com/geanhu/cme-
480 movie-analysis-2024.
481
482 **Acknowledgements**
483
484 We thank all members of the Drubin/Barnes laboratory for their help and support. We thank
485 Randy Schekman for allowing one of us (JMN) to perform lipid binding experiments for this
486 study. Yuichiro Iwamoto and Ross Pedersen provided constructive feedback and careful reading
487 of our manuscript. We thank Andrew Wong for his assistance in generating point mutant strains.
488 We are grateful to Constantine Bartolutti and Cyrus Ruediger of the Elçin Ünal/Gloria Brar
489 laboratory for their assistance with CRISPR/Cas9 methodology and for sharing the necessary
490 reagents. In addition, thank you to James Mester for conducting the Nikon NSPARC imaging
491 experiments. This work was supported by NIH grant R35GM118149 (D.G. Drubin).

492 **Figure Legends**
493
494 **FIGURE 1:** Spatiotemporal localization of fluorescent protein-tagged Snc1 and Snc2 expressed
495 from their endogenous genomic loci in normal, drug-treated, and mutant cells. **A.** Maximum
496 intensity projections of Airyscan confocal z-stacks of fixed yeast cells expressing GFP-Snc1 (with
497 intron removed from the *SNC1* gene) and GFP-Snc2, respectively. **B.** Maximum intensity
498 projections from a time-lapse movie of cells expressing GFP-Snc2 and Sla1-mScarlet acquired
499 using a Nikon confocal microscope equipped with an NSPARC detector (see Materials and
500 Methods). Here two budded cells and one unbudded cell are outlined. **C.** Montages of time-
501 lapse GFP-Snc2 live-cell NSPARC movies at different stages of cell growth. First row is an
502 expanded image of the bud in the second row. Time interval between each frame is 1.2
503 seconds. White and yellow arrows in the first and second rows identify unique translating Snc2-
504 positive puncta in daughter and mother cells, respectively. **D.** Circumferential kymographs made
505 from 3-minute NSPARC movies of cells expressing GFP-Snc2 and Sla1-mScarlet in different cell
506 regions and stages of cell growth. White, yellow, and cyan arrows denote unique Snc2/Sla1
507 interaction events in daughter, mother, and unbudded cells, respectively. Temporal resolution is
508 ~0.6 seconds. **E.** Still frames from time-lapse Airyscan confocal microscopy movies of wild-type
509 cells expressing GFP-Snc2 and treated with 50 µM CK-666 for 30 minutes, or 2 minutes after
510 washing out the inhibitor (cells in each column are different). **F.** Still frames from widefield time-
511 lapse movies of cells carrying various mutant GFP-Snc2 alleles.
512
513 **FIGURE S1: A.** Maximum intensity projections of Airyscan confocal z-stacks of fixed yeast cells
514 expressing GFP-Snc1 (with intron removed from the *SNC1* gene) and GFP-Snc2, respectively.
515 Budded cells are demarcated with arrows. **B.** Maximum intensity projections from a time-lapse
516 NSPARC movie of cells expressing GFP-Snc2 and Sla1-mScarlet. Budded cells are demarcated
517 with arrows. **C., D., E.** Three examples each of circumferential kymographs made from 3-minute
518 NSPARC movies of cells expressing GFP-Snc2 and Sla1-mScarlet in daughter, mother, and
519 unbudded cells, respectively. **F.** Circumferential kymographs made from a 4.5-minute NSPARC
520 movie of daughter cells expressing GFP-Snc2 and Sla1-mScarlet acquired directly after washout
521 of 50 µM CK-666 following 30 min. of treatment. White and yellow arrows denote distinct
522 Snc2/Sla1 interaction events.
523
524 **FIGURE S2: A.** Immunoblot displaying relative levels of V5-AID-tagged Snc1 and Snc2 expressed
525 from their normal promoters at their endogenous loci with anti-hexokinase loading control. **B.**
526 Serial dilutions of strains carrying indicated *snc* null and point mutants and fluorescent fusion
527 proteins on YPD. **C.** Immunoblot displaying relative levels of GFP-tagged Snc2 and snc2 V39A
528 M42A mutant in *SNC1* and *snc1Δ* backgrounds. **D.** Serial dilutions of strains carrying various
529 Yap1802 point mutations in a *yap1801Δ* background on YPD. **E.** Immunoblot displaying relative
530 levels of GFP-tagged Yap1802 point mutants. **F.** Liposome flotation assays with purified
531 truncated Yap1802 and yap1802 K21E K23E ANTH domains, two different replicates with
532 different protein amounts loaded. Liposomes were made with a molar composition of 38%
533 DOPC, 20% POPE, 20% DOPS, 3% PI(4,5)P_2, 0.5% TexasRed-PE, and 18.5% cholesterol. Relative
534 binding was computed for each replicate with one exposure optimized for the input and one
535 optimized for the buoyant fraction. Effective concentrations and binding fractions of the two

536 ANTH proteins were determined using densitometry in relation to the known His_6-HaloTag
537 concentration in each replicate using a single optimized exposure. Error bars for all
538 immunoblots represent standard deviation. **** indicates $p < 0.0001$.
539
540 **MOVIES S1 and S2:** Snc2 interacts with the endocytic machinery in a complex manner. Three-
541 minute movies acquired using a Nikon confocal microscope equipped with an NSPARC detector
542 (see Materials and Methods) of live cells expressing GFP-Snc2 (green) and Sla1-mScarlet
543 (magenta), both from the endogenous promoter and locus from the endogenous promoter and
544 locus in an *snc1Δ* background. Moving arrowheads track distinct Snc2-positive compartments.
545 **Movie S1:** first, a compartment translocating from one location on the plasma membrane to
546 another in a daughter cell, and second, two compartments in the mother cell that move
547 directionally from the cytosol to the bud neck. **Movie S2:** Moving arrowheads track distinct
548 interaction events between GFP-Snc2 and Sla1-mScarlet: first and second at the daughter cell
549 cortex, and third in a mother cell. Acquisition temporal resolution is ~0.6 seconds, playback rate
550 is 27 frames per second. Scale bar is 2 µm.
551
552 **FIGURE 2:** Yap1801/2 is recruited to the daughter cortex by Snc1/2 and negatively charged
553 lipids. **A.** Sequence alignment for human CALM and *S. cerevisiae* Yap1802. Red fill indicates
554 direct matches, and red characters indicate shared residue characteristics (Robert and Gouet,
555 2014). **B.** Alphafold2 multimer analysis of the ANTH domain of Yap1802 and Snc2, with key
556 residues highlighted in red. **C.** Maximum intensity projections from 6-minute widefield
557 microscopy movies of cells expressing various Yap1802 wild-type or point-mutant alleles, 3x PM
558 refers to the K21E K23E L203S triple point mutant. **D.** Circumferential kymographs made from 6-
559 minute widefield microscopy movies of Yap1802-GFP point mutants in medium-budded
560 daughter cells. Temporal resolution is 2 seconds. **E.** Mean intensities of Yap1802-GFP point
561 mutant line profiles from daughter cell cortexes as in **C.** Right to left, n = 35, 32, 23, 22 **F.**
562 Quantification of Yap1802-GFP point mutant lifetimes. **G.** Maximum intensity projections from
563 3-minute Airyscan confocal microscopy time-lapse movies of cells expressing wild-type Yap1802
564 or point mutants and mScarlet-Snc2. Temporal resolution of movies was ~3.7 seconds. Right to
565 left, n = 127, 129, 106, 97. **H.** Mean intensities of mScarlet-Snc2 line profiles from mother cell
566 cortexes as in **G.** Right to left, n = 17, 15, 17, 14. Groups in **E**, **F**, and **H** were compared using one-
567 way ANOVA. Center and error bars are mean and 95% confidence interval, *** indicates $0.001 >$
568 $p > 0.0001$, and **** indicates $p < 0.0001$.
569
570 **FIGURE S3: A.** GFP line traces of daughter cells as in **C** from wild-type and Yap1802 point mutant
571 maximum intensity projections for the same strains used in **Figure 2C**. **B.** mScarlet-Snc2 line
572 traces from maximum intensity projections of mother cells as in **Figure 2G** expressing Yap1802
573 wild-type protein or point mutants. For each plot, each trace from individual cells was
574 interpolated to match the mean length of cells in the wild-type cohort. Outlines represent a
575 95% confidence interval for each point in the trace, annotated microscopy images display
576 examples of individual line traces used. **C.** Maximum intensity projections of widefield z-stacks
577 of live cells expressing yap1802 3x PM-GFP and Ede1-mScarlet in a *yap1801Δ* background.
578 Colocalization is denoted with arrows.
579

580 **FIGURE 3**: **A.** Model for how interaction between synaptobrevin-like v-SNARES Snc1/2 and the
581 CME adaptor proteins Yap1801/2 contributes to CME site initiation and links endocytosis to
582 polarized exocytosis. Cdc42-nucleated actin cables enable directional transport of vesicles
583 toward the daughter bud tip, with fusion near the bud tip assisted by the exocyst vesicle
584 tethering complex. This localized secretion enriches the daughter plasma membrane in Snc1/2,
585 which, in concert with anionic phospholipids, recruit Yap1801/2 to internalize Snc1/2 via CME.
586 **B.** Model for Snc1/2 and anionic phospholipid coincidence detection, enabling robust
587 Yap1801/2 recruitment. Each individual Yap1802 mutant displays defects in recruitment when
588 compared to wild-type, an effect most pronounced in the triple point mutant. Created with
589 BioRender.com.

590 **References**

591 Adams, AE, and Pringle, JR (1984). Relationship of actin and tubulin distribution to bud growth
592 in wild-type and morphogenetic-mutant Saccharomyces cerevisiae. Journal of Cell Biology 98,
593 934–945.

594 Amberg, DC, Burke, DJ, and Strathern, JN (2005). Methods in Yeast Genetics: A Cold Spring
595 Harbor Laboratory Course Manual, Cold Spring Harbor, NY: Cold Spring Harbor Laboratory Press.

596 Anand, R, Memisoglu, G, and Haber, J (2017). Cas9-mediated gene editing in Saccharomyces
597 cerevisiae. Protocol Exchange.

598 Best, JT, Xu, P, McGuire, JG, Leahy, SN, and Graham, TR (2020). Yeast synaptobrevin, Snc1,
599 engages distinct routes of postendocytic recycling mediated by a sorting nexin, Rcy1-COPI, and
600 retromer. Molecular Biology of the Cell 31, 944–962.

601 Brach, T, Godlee, C, Moeller-Hansen, I, Boeke, D, and Kaksonen, M (2014). The initiation of
602 clathrin-mediated endocytosis is mechanistically highly flexible. Current Biology 24, 548–554.

603 Bradford, MK, Whitworth, K, and Wendland, B (2015). Pan1 regulates transitions between
604 stages of clathrin-mediated endocytosis. MBoC 26, 1371–1385.

605 Burri, L, and Lithgow, T (2004). A Complete Set of SNAREs in Yeast. Traffic 5, 45–52.

606 Burston, HE, Maldonado-Báez, L, Davey, M, Montpetit, B, Schluter, C, Wendland, B, and
607 Conibear, E (2009). Regulators of yeast endocytosis identified by systematic quantitative
608 analysis. Journal of Cell Biology 185, 1097–1110.

609 Carroll, SY, Stimpson, HEM, Weinberg, J, Toret, CP, Sun, Y, and Drubin, DG (2012). Analysis of
610 yeast endocytic site formation and maturation through a regulatory transition point. Molecular
611 Biology of the Cell 23, 657–668.

612 Carroll, SY, Stirling, PC, Stimpson, HEM, Gießelmann, E, Schmitt, MJ, and Drubin, DG (2009). A
613 Yeast Killer Toxin Screen Provides Insights into A/B Toxin Entry, Trafficking, and Killing
614 Mechanisms. Developmental Cell 17, 552–560.

615 Cocucci, E, Aguet, F, Boulant, S, and Kirchhausen, T (2012). The First Five Seconds in the Life of a
616 Clathrin-Coated Pit. Cell 150, 495–507.

617 Cortesio, CL, Lewellyn, EB, and Drubin, DG (2015). Control of lipid organization and actin
618 assembly during clathrin-mediated endocytosis by the cytoplasmic tail of the rhomboid protein
619 Rbd2. MBoC 26, 1509–1522.

620 Daetwyler, S, Modes, CD, and Fiolka, R (2020). Fiji plugin for annotating movies with custom
621 arrows. Biology Open 9, bio056200.

622 Delattre, S (2023). Igniting New Confocal Imaging Potential – Nikon AX R Series with NSPARC.
623 Microscopy Today 31, 23–27.

624 Field, C, and Schekman, R (1980). Localized secretion of acid phosphatase reflects the pattern of
625 cell surface growth in saccharomyces cerevisiae. Journal of Cell Biology 86, 123–128.

626 Ford, MGJ, Pearse, BMF, Higgins, MK, Vallis, Y, Owen, DJ, Gibson, A, Hopkins, CR, Evans, PR, and
627 McMahon, HT (2001). Simultaneous binding of PtdIns (4,5) P2 and clathrin by AP180 in the
628 nucleation of clathrin lattices on membranes. Science 291, 1051–1055.

629 Godlee, C, and Kaksonen, M (2013). From uncertain beginnings: Initiation mechanisms of
630 clathrin-mediated endocytosis. Journal of Cell Biology 203, 717–725.

631 Goode, BL, Eskin, JA, and Wendland, B (2015). Actin and Endocytosis in Budding Yeast. Genetics
632 199, 315–358.

633 Grote, E, Vlacich, G, Pypaert, M, and Novick, PJ (2000). A snc1 endocytosis mutant: Phenotypic
634 analysis and suppression by overproduction of dihydrosphingosine phosphate lyase. Molecular
635 Biology of the Cell 11, 4051–4065.

636 Gurunathan, S, Chapman-Shimshoni, D, Trajkovic, S, and Gerst, JE (2000). Yeast exocytic v-
637 SNAREs confer endocytosis. Molecular Biology of the Cell 11, 3629–3643.

638 Gurunathan, S, Marash, M, Weinberger, A, and Gerst, JE (2002). t-SNARE Phosphorylation
639 Regulates Endocytosis in Yeast. MBoC 13, 1594–1607.

640 Hetrick, B, Han, MS, Helgeson, LA, and Nolen, BJ (2013). Small Molecules CK-666 and CK-869
641 Inhibit Actin-Related Protein 2/3 Complex by Blocking an Activating Conformational Change.
642 Chemistry & Biology 20, 701–712.

643 Kaplan, C, and Ewers, H (2015). Optimized sample preparation for single-molecule localization-
644 based superresolution microscopy in yeast. Nature Protocols 2015 10:7 10, 1007–1021.

645 Katz, L, Hanson, PI, Heuser, JE, and Brennwald, P (1998). Genetic and morphological analyses
646 reveal a critical interaction between the C-termini of two SNARE proteins and a parallel four
647 helical arrangement for the exocytic SNARE complex. The EMBO Journal 17, 6200–6209.

648 Kreis, TE, Lowe, M, and Pepperkok, R (1995). COPs regulating membrane traffic. Annu Rev Cell
649 Dev Biol 11, 677–706.

650 Kunkel, TA (1985). Rapid and efficient site-specific mutagenesis without phenotypic selection.
651 Proceedings of the National Academy of Sciences 82, 488–492.

652 Kurokawa, K, Ishii, M, Suda, Y, Ichihara, A, and Nakano, A (2013). Live Cell Visualization of Golgi
653 Membrane Dynamics by Super-resolution Confocal Live Imaging Microscopy. Methods in Cell
654 Biology 118, 235–242.

655 Layton, AT, Savage, NS, Howell, AS, Carroll, SY, Drubin, DG, and Lew, DJ (2011). Modeling Vesicle
656 Traffic Reveals Unexpected Consequences for Cdc42p-Mediated Polarity Establishment. Current
657 Biology 21, 184–194.

658 Lewis, MJ, Nichols, BJ, Prescianotto-Baschong, C, Riezman, H, and Pelham, HRB (2000). Specific
659 Retrieval of the Exocytic SNARE Snc1p from Early Yeast Endosomes. MBoC 11, 23–38.

660 Lipson, D, Raz, T, Kieu, A, Jones, DR, Giladi, E, Thayer, E, Thompson, JF, Letovsky, S, Milos, P, and
661 Causey, M (2009). Quantification of the yeast transcriptome by single-molecule sequencing.
662 Nature Biotechnology 27, 652–658.

663 Longtine, MS, Mckenzie III, A, Demarini, DJ, Shah, NG, Wach, A, Brachat, A, Philippsen, P, and
664 Pringle, JR (1998). Additional modules for versatile and economical PCR-based gene deletion
665 and modification in Saccharomyces cerevisiae. Yeast 14, 953–961.

666 Lu, R, and Drubin, DG (2017). Selection and stabilization of endocytic sites by Ede1, a yeast
667 functional homologue of human Eps15. MBoC 28, 567–575.

668 Ma, M, and Burd, CG (2019). Retrograde trafficking and quality control of yeast synaptobrevin,
669 Snc1, are conferred by its transmembrane domain. Molecular Biology of the Cell 30, 1729–1742.

670 Maldonado-Báez, L, Dores, MR, Perkins, EM, Drivas, TG, Hicke, L, and Wendland, B (2008).
671 Interaction between Epsin/Yap180 adaptors and the scaffolds Ede1/Pan1 is required for
672 endocytosis. Molecular Biology of the Cell 19, 2936–2948.

673 Martin, SG, and Arkowitz, RA (2014). Cell polarization in budding and fission yeasts. FEMS
674 Microbiology Reviews 38, 228–253.

675 Martínez-Cagigal, V (2024). Shaded area error bar plot. MATLAB Central File Exchange. Available
676 at: https://www.mathworks.com/matlabcentral/fileexchange/58262-shaded-area-error-bar-
677 plot. Accessed May 11, 2024.

678 Meca, J, Massoni-Laporte, A, Martinez, D, Sartorel, E, Loquet, A, Habenstein, B, and McCusker, D
679 (2019). Avidity-driven polarity establishment via multivalent lipid–GTPase module interactions.
680 The EMBO Journal 38, e99652.

681 Mei, K, and Guo, W (2018). The exocyst complex. Current Biology 28, R922–R925.

682 Mei, K, Li, Y, Wang, S, Shao, G, Wang, J, Ding, Y, Luo, G, Yue, P, Liu, J-J, Wang, X, *et al.* (2018).
683 Cryo-EM structure of the exocyst complex. Nat Struct Mol Biol 25, 139–146.

684 Miller, SE, Sahlender, DA, Graham, SC, Höning, S, Robinson, MS, Peden, AA, and Owen, DJ
685 (2011). The Molecular Basis for the Endocytosis of Small R-SNAREs by the Clathrin Adaptor
686 CALM. Cell 147, 1118–1131.

687 Mirdita, M, Schütze, K, Moriwaki, Y, Heo, L, Ovchinnikov, S, and Steinegger, M (2022). ColabFold:
688 making protein folding accessible to all. Nat Methods 19, 679–682.

689 Ngo, JM, Williams, JK, Temoche-Diaz, MM, Murugupandiyan, A, and Schekman, R (2025). p62
690 sorts Lupus La and selected microRNAs into breast cancer-derived exosomes. J Cell Biol 225,
691 e202503087.

692 Pashkova, N, Gakhar, L, Yu, L, Schnicker, NJ, Minard, AY, Winistorfer, S, Johnson, IE, and Piper, RC
693 (2021). Anth domains within CALM, HIP1R, and Sla2 recognize ubiquitin internalization signals.
694 eLife 10.

695 Pedersen, RTA, and Drubin, DG (2019). Type I myosins anchor actin assembly to the plasma
696 membrane during clathrin-mediated endocytosis. Journal of Cell Biology 218, 1138–1147.

697 Pedersen, RTA, Hassinger, JE, Marchando, P, and Drubin, DG (2020). Spatial regulation of
698 clathrin-mediated endocytosis through position-dependent site maturation. Journal of Cell
699 Biology 219.

700 Pruyne, D, and Bretscher, A (2000a). Polarization of cell growth in yeast: I. Establishment and
701 maintenance of polarity states. Journal of Cell Science 113, 365–375.

702 Pruyne, D, and Bretscher, A (2000b). Polarization of cell growth in yeast II. The role of the
703 cortical actin cytoskeleton. Journal of Cell Science 113, 571–585.

704 Robert, X, and Gouet, P (2014). Deciphering key features in protein structures with the new
705 ENDscript server. Nucleic Acids Research 42, W320–W324.

706 Saheki, Y, and Camilli, PD (2012). Synaptic Vesicle Endocytosis. Cold Spring Harb Perspect Biol 4,
707 a005645.

708 Shen, D, Yuan, H, Hutagalung, A, Verma, A, Kümmel, D, Wu, X, Reinisch, K, McNew, JA, and
709 Novick, P (2013). The synaptobrevin homologue Snc2p recruits the exocyst to secretory vesicles
710 by binding to Sec6p. Journal of Cell Biology 202, 509–526.

711 Stauffer, B, and Powers, T (2015). Target of rapamycin signaling mediates vacuolar fission caused
712 by endoplasmic reticulum stress in Saccharomyces cerevisiae. Mol Biol Cell 26, 4618–4630.

713 Stimpson, HEM, Toret, CP, Cheng, AT, Pauly, BS, and Drubin, DG (2009). Early-Arriving Syp1p and
714 Ede1p Function in Endocytic Site Placement and Formation in Budding Yeast. MBoC 20, 4640–
715 4651.

716 Stringer, C, Wang, T, Michaelos, M, and Pachitariu, M (2021). Cellpose: a generalist algorithm for
717 cellular segmentation. Nat Methods 18, 100–106.

718 Sun, Y, and Drubin, DG (2012). The functions of anionic phospholipids during clathrin-mediated
719 endocytosis site initiation and vesicle formation. Journal of Cell Science 125, 6157–6165.

720 Sun, Y, Kaksonen, M, Madden, DT, Schekman, R, and Drubin, DG (2005). Interaction of Sla2p's
721 ANTH domain with PtdIns(4,5)P2 is important for actin-dependent endocytic internalization.
722 Molecular Biology of the Cell 16, 717–730.

723 Sun, Y, Leong, NT, Jiang, T, Tangara, A, Darzacq, X, and Drubin, DG (2017). Switch-like Arp2/3
724 activation upon WASP and WIP recruitment to an apparent threshold level by multivalent linker
725 proteins in vivo. eLife 6.

726 Sun, Y, Leong, NT, Wong, T, and Drubin, DG (2015). A Pan1/End3/Sla1 complex links Arp2/3-
727 mediated actin assembly to sites of clathrin-mediated endocytosis. Molecular Biology of the Cell
728 26, 3841–3856.

729 Sun, Y, Yeam, A, Kuo, J, Iwamoto, Y, Hu, G, and Drubin, DG (2024). The conserved protein
730 adaptors CALM/AP180 and FCHo1/2 cooperatively recruit Eps15 to promote the initiation of
731 clathrin-mediated endocytosis in yeast. PLOS Biology 22.

732 Taylor, MJ, Perrais, D, and Merrifield, CJ (2011). A High Precision Survey of the Molecular
733 Dynamics of Mammalian Clathrin-Mediated Endocytosis. PLOS Biology 9, e1000604.

734 Toshima, JY, Toshima, J, Kaksonen, M, Martin, AC, King, DS, and Drubin, DG (2006). Spatial
735 dynamics of receptor-mediated endocytic trafficking in budding yeast revealed by using
736 fluorescent alpha-factor derivatives. Proceedings of the National Academy of Sciences of the
737 United States of America 103, 5793–5798.

738 Valdez-Taubas, J, and Pelham, HRB (2003). Slow Diffusion of Proteins in the Yeast Plasma
739 Membrane Allows Polarity to Be Maintained by Endocytic Cycling. Current Biology 13, 1636–
740 1640.

741 Williams, JK, Ngo, JM, Murugupandiyan, A, Croall, DE, Hartzell, HC, and Schekman, R (2025).
742 Calpains orchestrate secretion of annexin-containing microvesicles during membrane repair.
743 Journal of Cell Biology 224, e202408159.

744

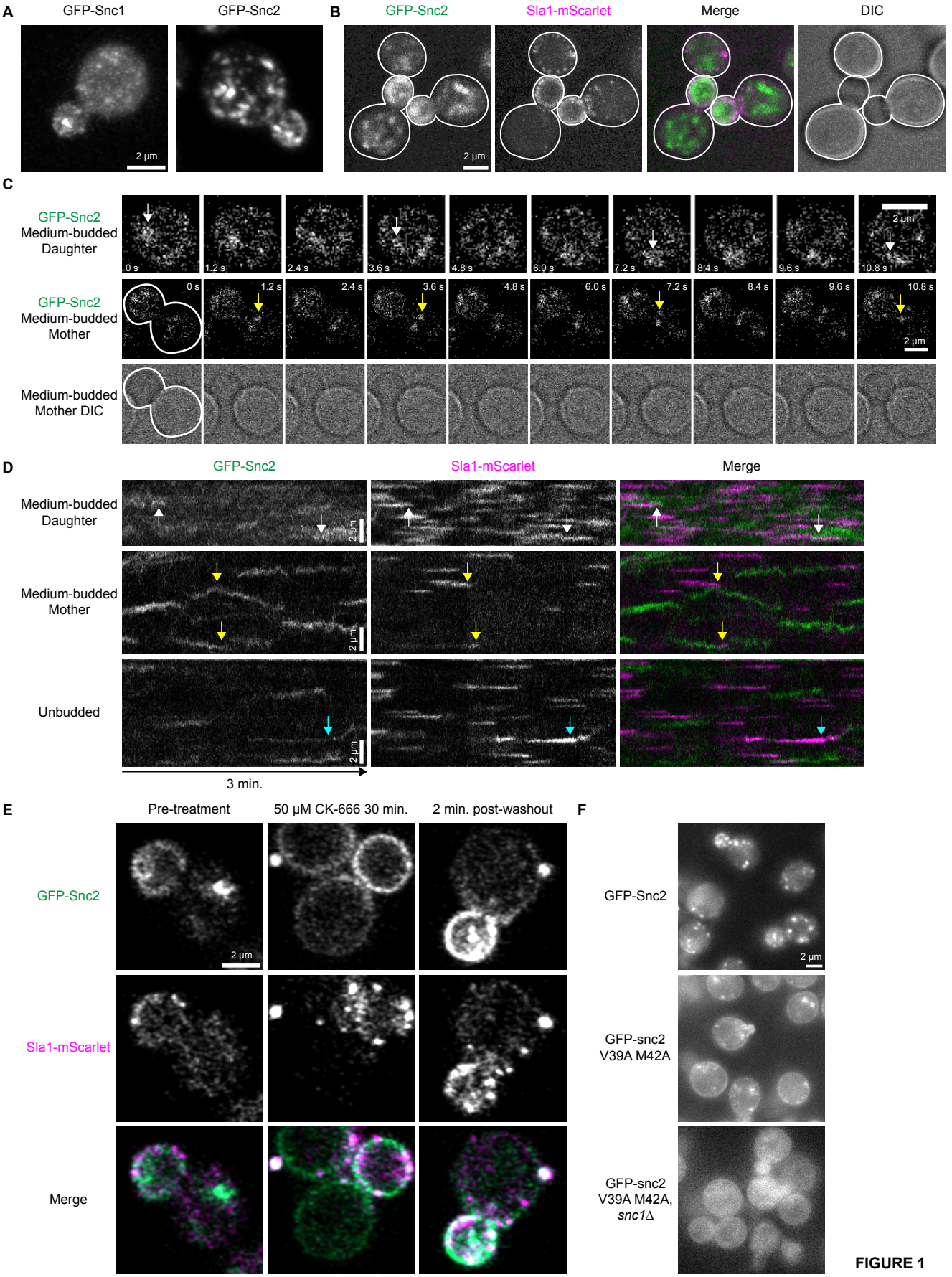
A
GFP-Snc1
GFP-Snc2
2 µm
B
GFP-Snc2
Sla1-mScarlet
Merge
DIC
2 µm
C
GFP-Snc2
Medium-budded
Daughter
GFP-Snc2
Medium-budded
Mother
Medium-budded
Mother DIC
0 s
1.2 s
2.4 s
3.6 s
4.8 s
6.0 s
7.2 s
8.4 s
9.6 s
10.8 s
2 µm
D
GFP-Snc2
Sla1-mScarlet
Merge
Medium-budded
Daughter
Medium-budded
Mother
Unbudded
2 µm
3 min.
E
Pre-treatment
50 µM CK-666 30 min.
2 min. post-washout
GFP-Snc2
Sla1-mScarlet
Merge
2 µm
F
GFP-Snc2
GFP-snc2
V39A M42A
GFP-snc2
V39A M42A,
snc1Δ
2 µm

FIGURE 1

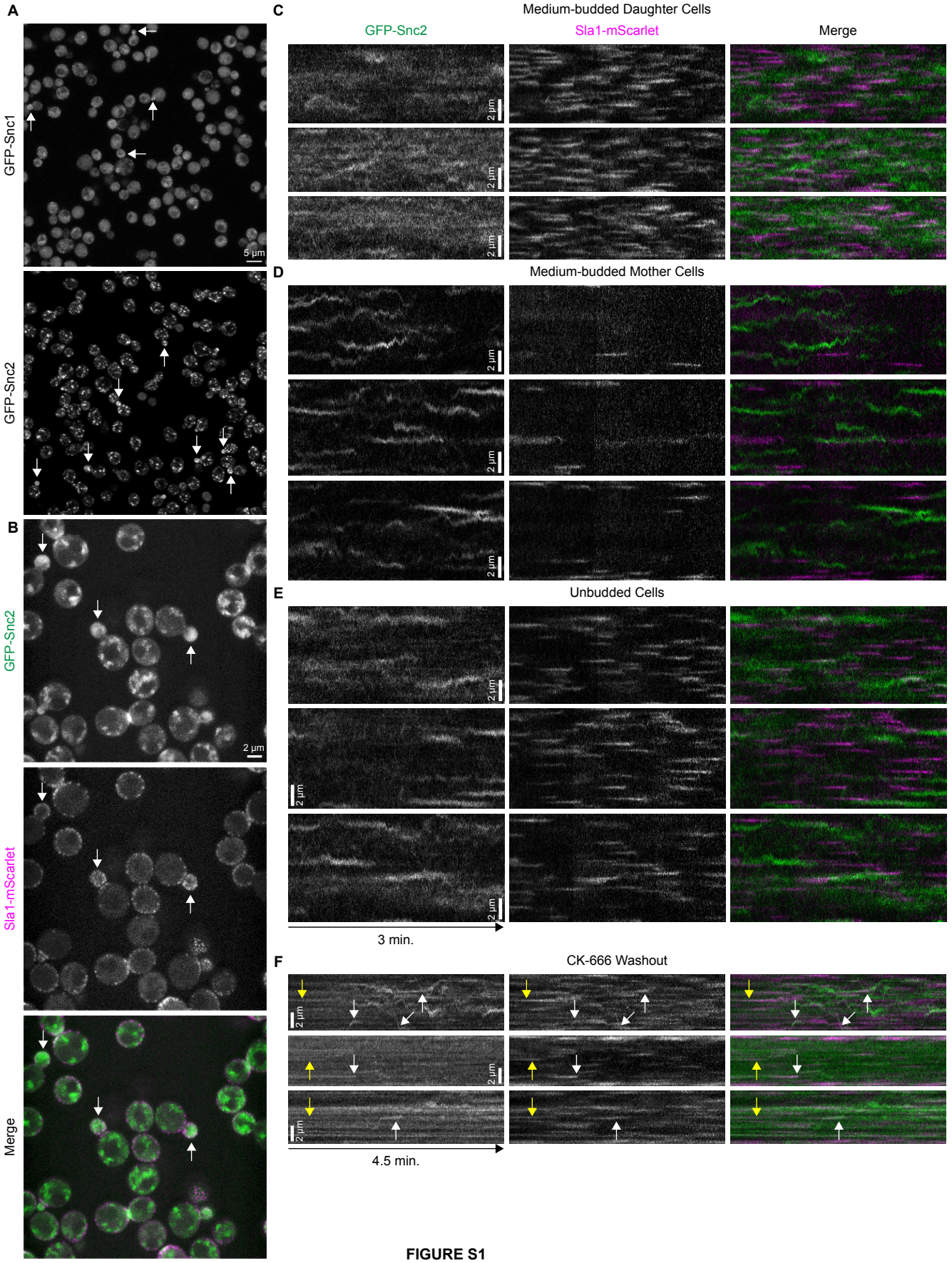
A
GFP-Snc1
5 µm
GFP-Snc2
B
GFP-Snc2
2 µm
Sla1-mScarlet
Merge
C
Medium-budded Daughter Cells
GFP-Snc2
Sla1-mScarlet
Merge
2 µm
D
Medium-budded Mother Cells
2 µm
E
Unbudded Cells
2 µm
3 min.
F
CK-666 Washout
2 µm
4.5 min.

FIGURE S1

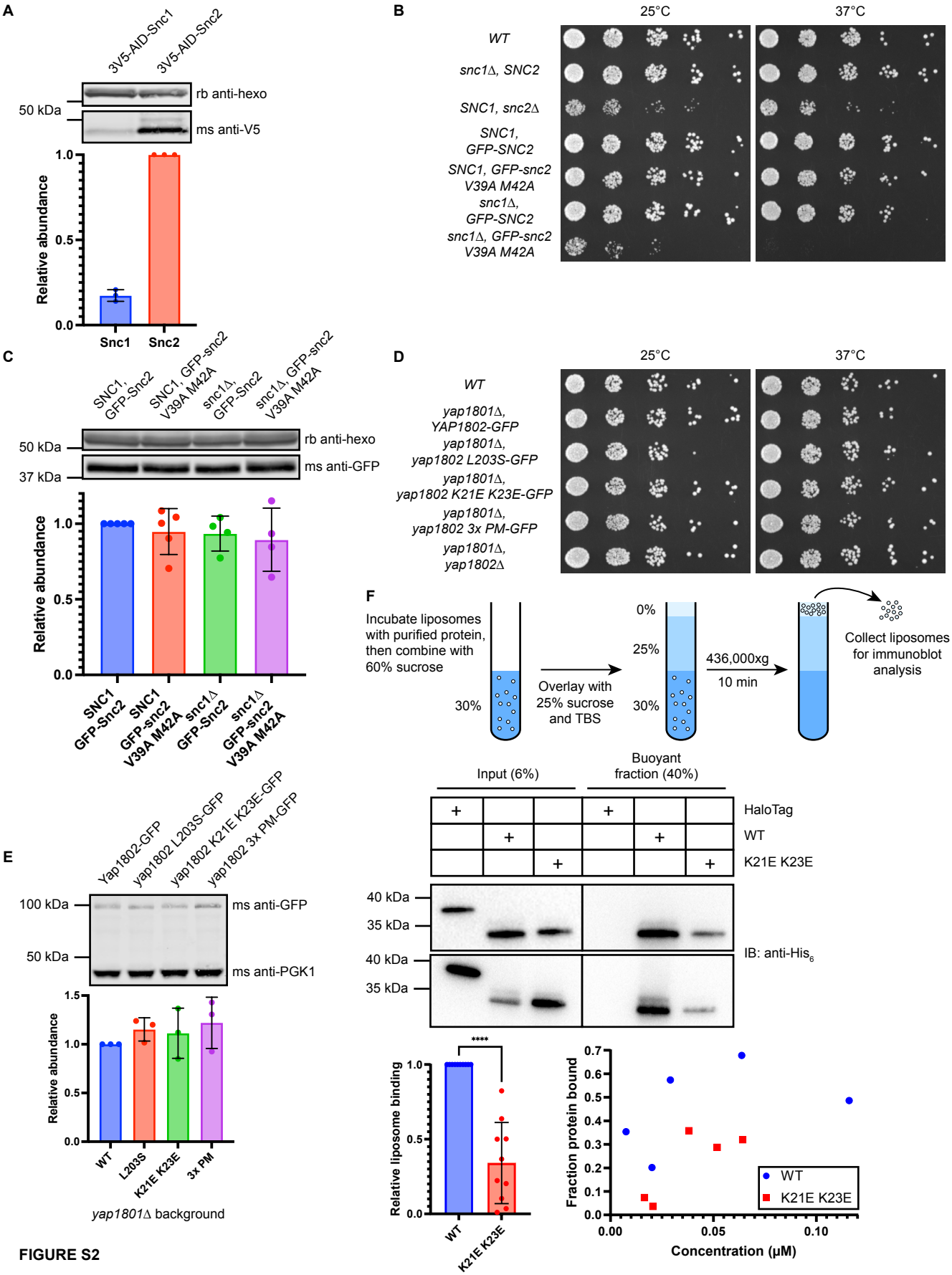
A
3V5-AID-Snc1
3V5-AID-Snc2
50 kDa
rb anti-hexo
ms anti-V5
Relative abundance
1.0
0.5
0.0
Snc1
Snc2
B
25°C
37°C
WT
snc1Δ, SNC2
SNC1, snc2Δ
SNC1, GFP-SNC2
SNC1, GFP-snc2 V39A M42A
snc1Δ, GFP-SNC2
snc1Δ, GFP-snc2 V39A M42A
C
SNC1, GFP-Snc2
SNC1, GFP-snc2 V39A M42A
snc1Δ, GFP-Snc2
snc1Δ, GFP-snc2 V39A M42A
50 kDa
37 kDa
rb anti-hexo
ms anti-GFP
Relative abundance
1.0
0.5
0.0
SNC1 GFP-Snc2
SNC1 GFP-snc2 V39A M42A
snc1Δ GFP-Snc2
snc1Δ GFP-snc2 V39A M42A
D
25°C
37°C
WT
yap1801Δ, YAP1802-GFP
yap1801Δ, yap1802 L203S-GFP
yap1801Δ, yap1802 K21E K23E-GFP
yap1801Δ, yap1802 3x PM-GFP
yap1801Δ, yap1802Δ
E
Yap1802-GFP
yap1802 L203S-GFP
yap1802 K21E K23E-GFP
yap1802 3x PM-GFP
100 kDa
50 kDa
ms anti-GFP
ms anti-PGK1
Relative abundance
1.5
1.0
0.5
0.0
WT
L203S
K21E K23E
3x PM
yap1801Δ background
F
Incubate liposomes with purified protein, then combine with 60% sucrose
30%
Overlay with 25% sucrose and TBS
0%
25%
30%
436,000xg
10 min
Collect liposomes for immunoblot analysis
Input (6%)
Buoyant fraction (40%)
HaloTag
WT
K21E K23E
40 kDa
35 kDa
IB: anti-His6
****
Relative liposome binding
1.0
0.5
0.0
WT
K21E K23E
Fraction protein bound
0.7
0.6
0.5
0.4
0.3
0.2
0.1
0.0
0.00
0.05
0.10
Concentration (μM)
WT
K21E K23E

FIGURE S2

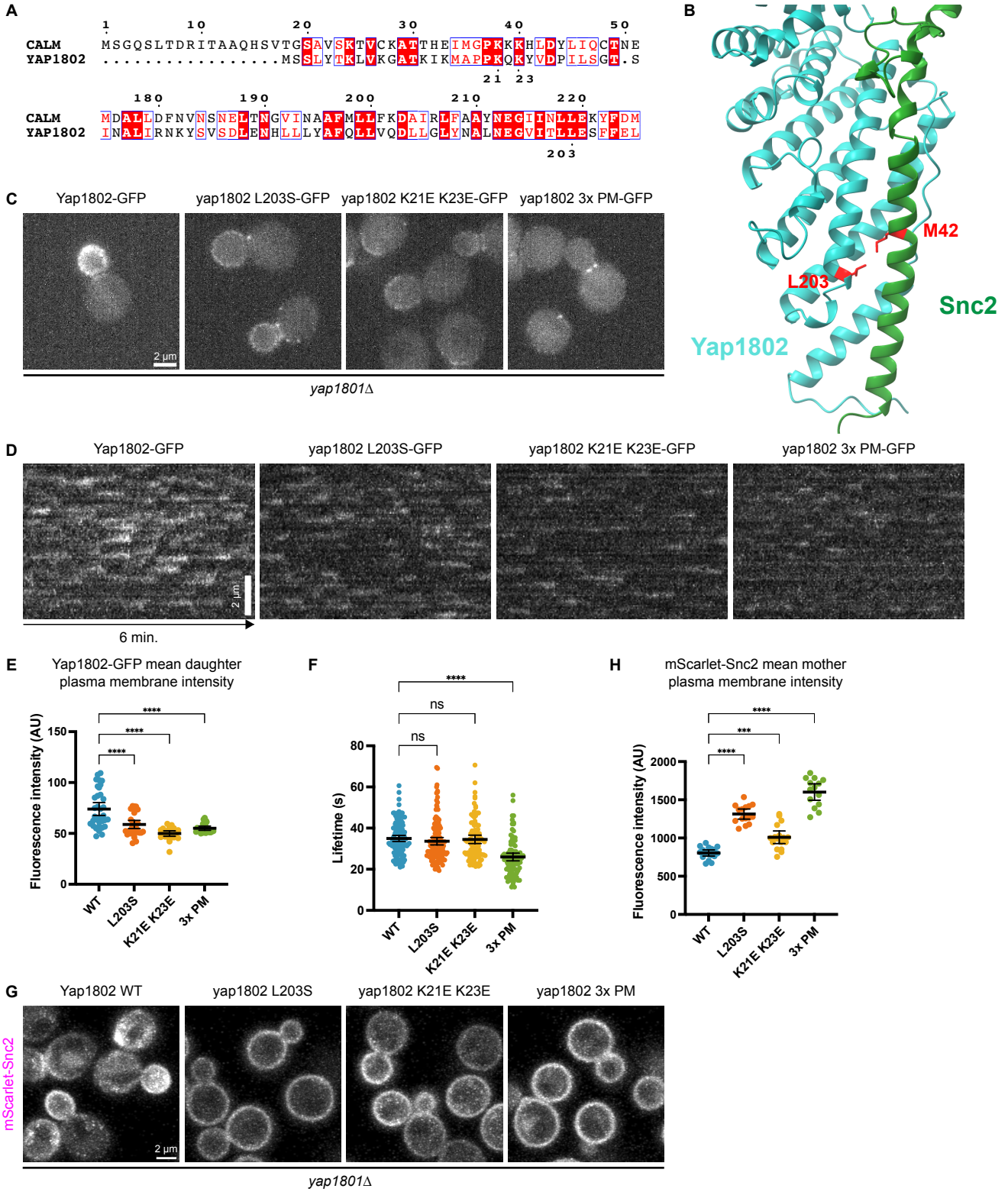
A
CALM
YAP1802
B
M42
L203
Snc2
Yap1802
C
Yap1802-GFP
yap1802 L203S-GFP
yap1802 K21E K23E-GFP
yap1802 3x PM-GFP
2 µm
yap1801Δ
D
Yap1802-GFP
yap1802 L203S-GFP
yap1802 K21E K23E-GFP
yap1802 3x PM-GFP
2 µm
6 min.
E
Yap1802-GFP mean daughter plasma membrane intensity
Fluorescence intensity (AU)
WT
L203S
K21E K23E
3x PM
F
Lifetime (s)
ns
ns
WT
L203S
K21E K23E
3x PM
H
mScarlet-Snc2 mean mother plasma membrane intensity
Fluorescence intensity (AU)
WT
L203S
K21E K23E
3x PM
G
Yap1802 WT
yap1802 L203S
yap1802 K21E K23E
yap1802 3x PM
mScarlet-Snc2
2 µm
yap1801Δ

FIGURE 2

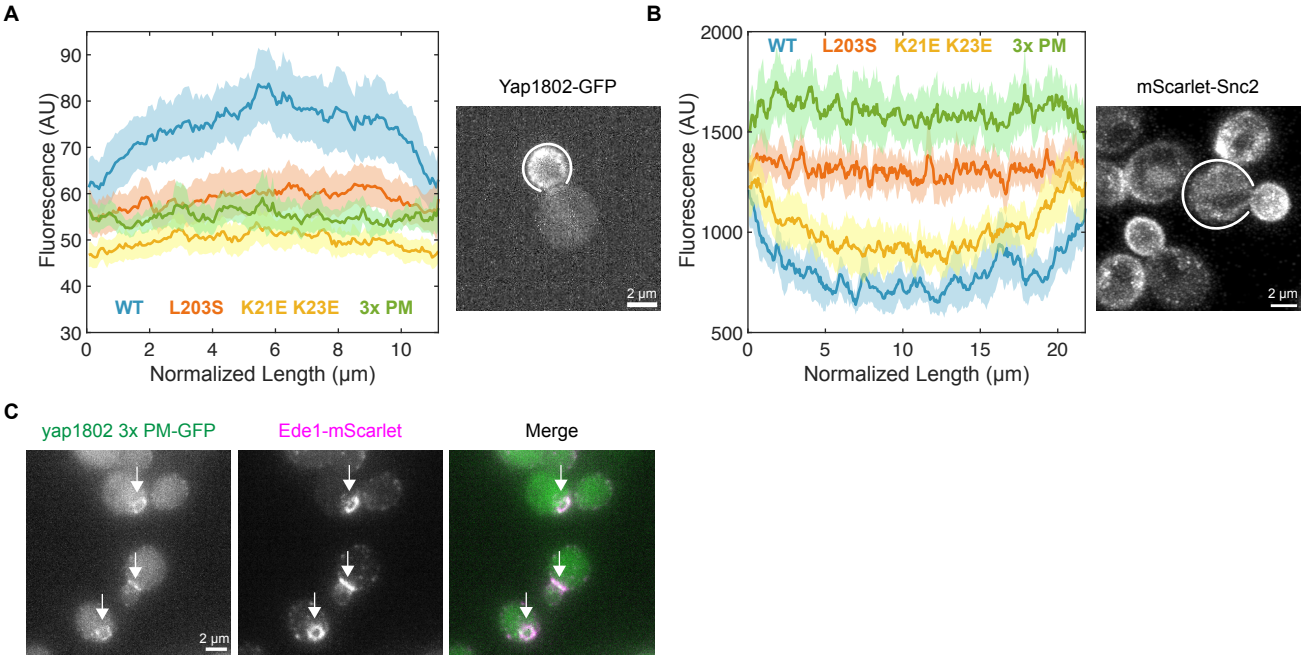
A
Fluorescence (AU)
Normalized Length (μm)
WT
L203S
K21E K23E
3x PM
Yap1802-GFP
2 μm
B
Fluorescence (AU)
Normalized Length (μm)
WT
L203S
K21E K23E
3x PM
mScarlet-Snc2
2 μm
C
yap1802 3x PM-GFP
Ede1-mScarlet
Merge
2 μm

FIGURE S3

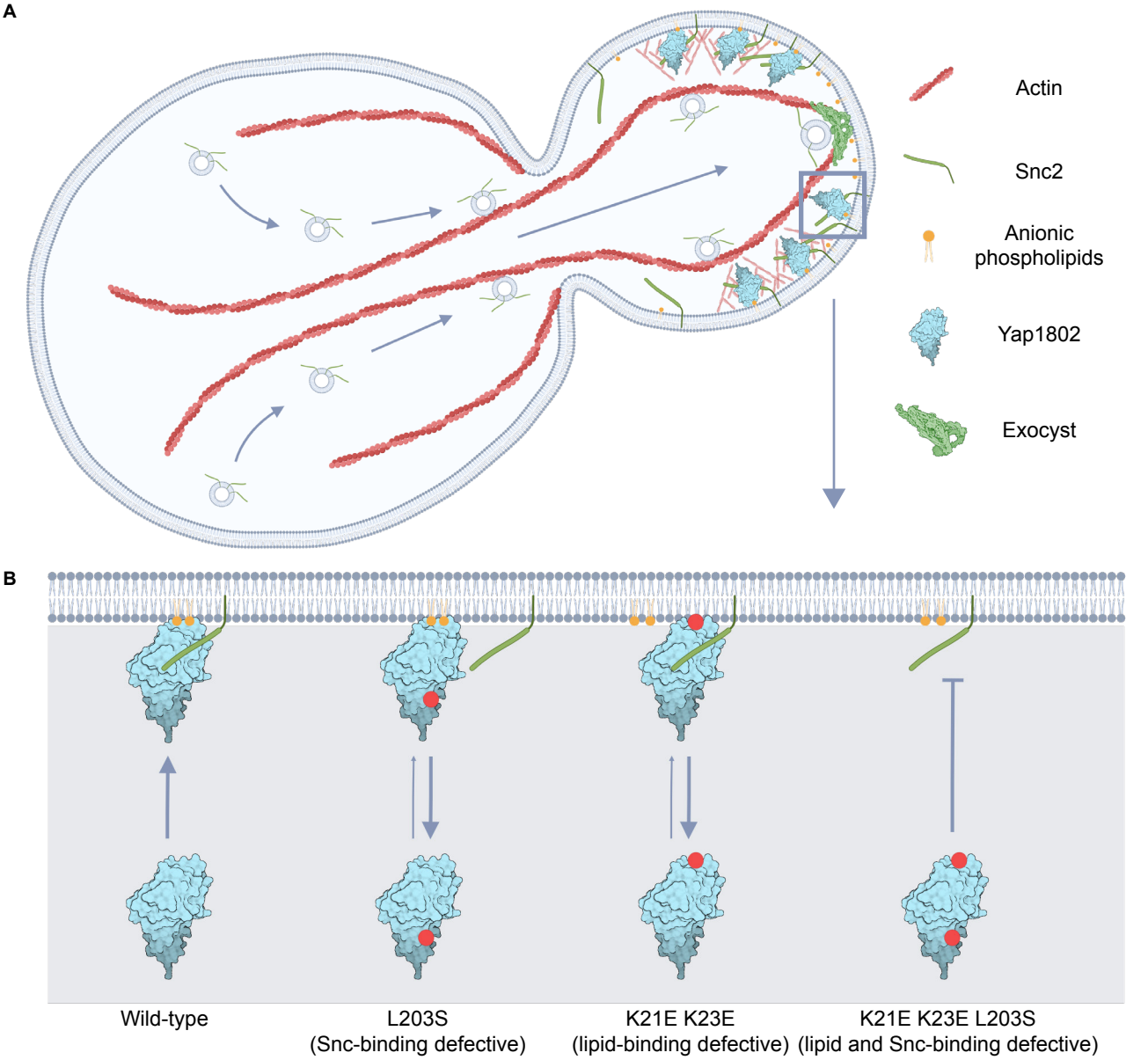
A
Actin
Snc2
Anionic phospholipids
Yap1802
Exocyst
B
Wild-type
L203S
(Snc-binding defective)
K21E K23E
(lipid-binding defective)
K21E K23E L203S
(lipid and Snc-binding defective)

FIGURE 3